AIAA JOURNAL
Vol. 50, No. 12, December 2012

X-HALE: A Very Flexible Unmanned Aerial Vehicle for Nonlinear Aeroelastic Tests

Carlos E. S. Cesnik,* Patrick J. Senatore,† Weihua Su,‡ and Ella M. Atkins§
University of Michigan, Ann Arbor, Michigan 48109-2140
and
Christopher M. Shearer¶
U.S. Air Force Institute of Technology, Wright-Patterson Air Force Base, Ohio 45433-7765

DOI: 10.2514/1.J051392

The University of Michigan has designed and built an unmanned aerial vehicle denoted X-HALE, which is aeroelastically representative of very flexible aircraft. The objective of this test bed is to collect unique data of the geometrically nonlinear aeroelastic response coupled with the flight dynamics to be used for future code validation. The aircraft presents specific aeroelastic features (e.g., coupled rigid/elastic body instability, large wing deflection during gust) that can be measured in flight. Moreover, the airframe construction choice is such that the elastic, inertial, and geometric properties can be well characterized. These are requirements driven by the need of the collected data to be used to support validation of coupled nonlinear aeroelastic/flight dynamics codes.

Nomenclature

c	=	chord, m
c_d	=	airfoil drag coefficient
c_l	=	airfoil lift coefficient
$c_{l\alpha}$	=	airfoil lift curve slope
c_m	=	airfoil moment coefficient
d	=	diameter, m
I_{ij}	=	cross-sectional mass moment of inertia, kg · m, $i, j = x, y, z$
I^c_{ij}	=	mass moment of inertia of concentrated mass, kg · m^2, $i, j = x, y, z$
k_{ij}	=	cross-sectional stiffness, $i, j = 1, 2, 3, 4$
m	=	mass per unit span, kg/m
mass	=	mass of concentrated mass, kg
x_{cg}, y_{cg}, z_{cg}	=	position of center of gravity of concentrated mass, m

I. Introduction

RECENT advances in airborne sensors and communication packages have given us the opportunity to place them at high altitudes for long periods of time. The missions include airborne intelligence, surveillance, and reconnaissance (ISR) for the military [1], network communication nodes for military and civilian usage, and general atmospheric research [2]. Because of the mission requirements, the aircraft platforms are characterized by high-aspect-ratio wings, and if existent, slender fuselages, resulting in very flexible vehicles. Improved mission capabilities such as longer loiter times, heavier payload, and greater range drive the demand for greater aerodynamic performance on those systems. Enhanced airframe performance is generally achieved through lightweight, flexible solutions. Modern high-altitude long-endurance (HALE) aircraft designs have become so lightweight and flexible that traditional (linear) design methods are no longer adequate, and nonlinear aeroelastic design methods are required to characterize structural and aeroelastic designs [3]. The wings may undergo large deformations during normal operating loads, exhibiting geometrically nonlinear behavior (Fig. 1).

In the last several years, the U.S. Air Force has been working on a new-generation intelligence, surveillance, and reconnaissance (ISR) platform called Sensorcraft. These large HALE aircraft have wing span of approximately 60 m. Three basic platform shapes have been considered: wing-body-tail, single-wing, and joined-wing configurations [1] (see Fig. 2). For high structural performance as required for long loiter times, these configurations will generally lead to very flexible aircraft. These flexibility effects may make the response of the vehicle very different from its rigid or linearized models [4]. Engineering analysis on very flexible vehicles will need to include geometrically nonlinear structural models for the primary structures to capture any large deformations that may appear under operational loads. Another characteristic of very flexible aircraft is very low frequencies of their natural structural vibration modes. Because of this, a strong coupling between the structural dynamics and the rigid-body (flight dynamics) characteristics of the vehicle should be expected.

More recently, Aurora Flight Sciences, Boeing Co., and Lockheed-Martin Co. have developed extreme long-duration HALE concepts [5]. The combination of high aerodynamic efficiency and low structural-to-weight fraction yields inherently flexible wings and nonlinear structural and flight dynamics. HALE aircraft are expected to be susceptible to large dynamic wing deformations at low frequencies, presenting a direct impact into the flight dynamic characteristics of the vehicle, as was seen in the Helios flight tests [6]. On June 26, 2003, NASA's Helios aircraft [6]:

HP03-2 took off at 10:06 a.m. local time from the Navy Pacific Missile Range Facility (PMRF) located on the island of Kauai, Hawaii. . . .At 10:22 a.m. and 10:24 a.m., the aircraft encountered turbulence and the wing dihedral became much larger than normal and mild pitch oscillations began but quickly damped out. At about 30 min into the flight, the aircraft encountered turbulence and morphed into an unexpected, persistent, high-dihedral configuration. As a result of the persistent high dihedral, the aircraft became

Presented at the 51st AIAA/ASME/ASCE/AHS/ASC Structures, Structural Dynamics, and Materials Conference, Orlando, FL, April 12–15, 2010; received 9 October 2011; revision received 18 December 2011; accepted for publication 31 December 2011.

*Professor, Department of Aerospace Engineering; cesnik@umich.edu. Fellow AIAA.
†Research Assistant, Department of Aerospace Engineering; senatorp@umich.edu. Member AIAA.
‡Post-Doctoral Research Fellow, Department of Aerospace Engineering; suw@umich.edu. Senior Member AIAA.
§Associate Professor, Department of Aerospace Engineering; ematkins@umich.edu. Associate Fellow AIAA.
¶Lt. Colonel, USAF, Department of Aeronautics and Astronautics; christopher.shearer@afit.edu. Member AIAA.

Fig. 1 Aerovironment's Helios (left) and Aurora Flight Sciences' Theseus (right) showing large wing deflections (Courtesy NASA Dryden).

Fig. 2 Three different Sensorcraft configurations [1].

unstable in a very divergent pitch mode in which the airspeed excursions from the nominal flight speed about doubled every cycle of the oscillation. The aircraft design airspeed was subsequently exceeded and the resulting high dynamic pressures caused the wing leading-edge secondary structure on the outer wing panels to fail and the solar cells and skin on the upper surface of the wing to rip off. The aircraft impacted the ocean within the confines of the PMRF test range and was destroyed. . . .The root causes of the mishap include: [A] lack of adequate analysis methods led to an inaccurate risk assessment of the effects of configuration changes leading to an inappropriate decision to fly an aircraft configuration highly sensitive to disturbances. . .[and] configuration changes to the aircraft, driven by programmatic and technological constraints, altered the aircraft from a spanloader to a highly point-loaded mass distribution on the same structure, significantly reducing design robustness and margins of safety.

The Helios accident highlighted our limited understanding and limited analytical tools necessary for designing very flexible aircraft and to potentially exploit aircraft flexibility. The primary root cause/recommendation from NASA [6] was:

[that] more advanced, multidisciplinary (structures, aeroelastic, aerodynamics, atmospheric, materials, propulsion, controls, etc.) time-domain analysis methods appropriate to highly flexible, morphing vehicles [be developed].

Nonlinear aeroelastic solvers have been under development to improve predictions of aircraft response, stability, and overall performance [4,7–14]. The body of work in the literature associated with the problem of nonlinear aeroelasticity coupled with nonlinear flight dynamics started developing at earnest in the 1990's. Without attempting to be comprehensive, what follows highlights some of the key contributions in the field. A more detailed review can be found in [4] and [13].

Early nonlinear aeroelastic work in very flexible aircraft was conducted by van Schoor and von Flotow [15]. Their work demonstrated the critical importance of including aircraft structural dynamics when analyzing aircraft flight dynamics of very flexible aircraft. Using linearized analysis about nonlinear equilibrium points, they showed a significant change in the classic rigid-body modes when flexible structural modeling is included. This leads to the conclusion that the coupled effects between these large deflection and vehicle flexibility and flight dynamics (e.g., roll controllability), as well as other aeroelastic effects (e.g., gust response, flutter instability), must be properly accounted for in a nonlinear aeroelastic formulation. Patil et al. [9] studied the aeroelasticity and flight dynamics of HALE aircraft. The results indicated that their behavior could be significantly changed due to the large deflection of the flexible wings. Moreover, a linear aeroelastic analysis based on the undeformed geometry may lead to errors when the wings are highly flexible. That study also showed a significant difference between the short-period and phugoid modes of a very flexible aircraft when comparing rigid-body, linear aeroelastic, and nonlinear aeroelastic dynamics. The short period and phugoid modes were obtained by linearizing the nonlinear dynamics about a nonlinear equilibrium. In a parallel effort, Drela [8] modeled a complete flexible aircraft as an assemblage of joined nonlinear beams. In his work, the aerodynamic model was a compressible vortex/source-lattice with wind-aligned trailing vorticity. The nonlinear equation was solved by using a full Newton method. Through simplifications of the model, the computational size was reduced for iterative preliminary design. Jones and his co-workers [16,17] have also worked on the HALE design. In their work, they described some design challenges associated with these vehicles. From their conclusion, it is shown that standard aircraft design techniques are no longer applicable for these high-aspect-ratio wings.

Besides the previously described work, Cesnik and his co-workers have developed a novel and practical solution to the coupled nonlinear aeroelasticity and flight dynamics of very flexible aircraft. Focusing on a reduced number of states to represent the complex nonlinear problem, the framework, named the University of Michigan's Nonlinear Aeroelastic Simulation Toolbox (UM/NAST), provides a suitable plant representation for control design. Several aeroelastic issues in high-altitude, long-endurance aircraft have been addressed, including nonlinear aeroelastic modeling [4,11], integral wing actuation for generating maneuver loads and overall nonlinear vehicle optimization of unconventional configurations [18], flutter-boundary enhancement [19], and gust-load alleviation [20].

All of these numerical efforts must eventually be validated against experimental data so they can be applied to new HALE aircraft concepts. The various components of most of the existing codes have been partially validated with limited experimental data coming from bench (e.g., [21–23]) and/or small-scale wind-tunnel tests (e.g., [24,25]). Some of the discipline components have also been compared against well-established numerical solutions (e.g., nonlinear composite-beam analyses, rigid flight dynamics, computational fluid

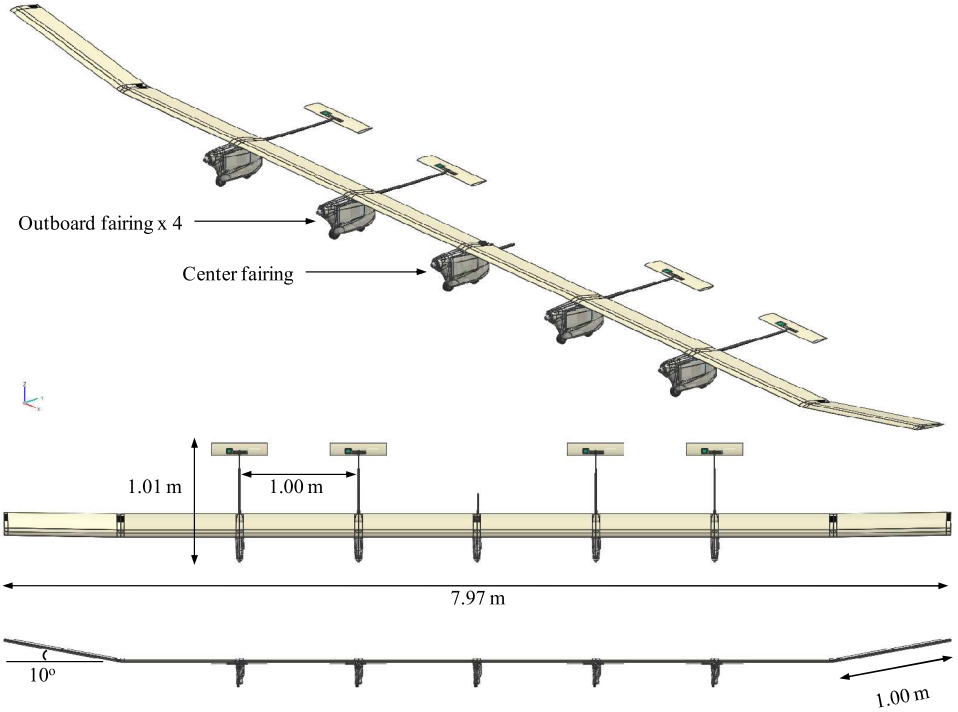

Fig. 3 Complete X-HALE CAD assembly: isometric, top, and front views.

dynamics). There has been, however, no validation of the integrated solution that brings the coupling effects between nonlinear aeroelasticity and flight dynamics, as no data are available for such exercise.

This paper describes the on-going effort to design and build a very flexible experimental remote-piloted aircraft named X-HALE. The purpose of X-HALE is to provide a platform to collect nonlinear aeroelastic-coupled, rigid-body flight dynamics data in support of nonlinear aeroelastic code validation. Moreover, it is also intended to be used as a platform to test nonlinear control laws. The X-HALE is expected to experience large deflections during flight, resulting in geometric nonlinearities. Furthermore, the X-HALE is designed to present an unstable but controllable Dutch roll coupled with the first flexible wing-bending mode. Time-accurate measurements of large in-flight vehicle deflections and control inputs and outputs will enable validation of nonlinear aeroelastic solvers. The following sections discuss the design and its expected main aeroelastic characteristics in details.

II. X-HALE Design, Integration, and Fabrication

The primary purpose of the X-HALE experiment is to generate data that can be used in support for validation of coupled nonlinear aeroelastic and flight simulation formulations. To this end, the system design and layout must produce an airframe that is consistent and measurable in both actual and simulated flight. Elastic, inertial, and aerodynamic properties must be well-characterized to reduce the uncertainties in modeling them. This requirement leads to design and manufacturing choices that simplify obtaining those properties and limit their variations. In addition, the need for the vehicle to present an unstable but controllable aeroelastic-coupled flight dynamics behavior adds considerable complexity to its design. Therefore, the vehicle must be stable in calm air and the instability should be excitable by large disturbances. The aircraft's very flexible structure should also be able to demonstrate large wing deformations (i.e., more than 25% semi-span tip deflections) without compromising its integrity. These unique requirements of the X-HALE experiment make its design very challenging. Structurally, the wing must be idealized and fabricated as a consistent composite slender structure (beam) to create a representative simulated model. To gather the required strain, control input, and flight attitude/rate data, a complex array of sensors and supporting data acquisition hardware and software must be integrated without impacting the wing's structural properties. This section will describe the composition of the X-HALE airframe and the integration methods used to guarantee similar flight and simulated platforms.

A. Airframe Layout

The X-HALE is a flexible, high-aspect-ratio, wing-boom-tail type aircraft. It has an 8-m span (constructed with eight identical 1-m sections) 0.2-m chord; four 0.83-m booms with horizontal tails attached and five motor pods with propellers, batteries, and processor boards (Fig. 3). X-HALE has a mass of 11 kg with an anticipated flight speed ranging from 10 to 19 m/s. Its main vehicle-sizing characteristics are presented in Table 1. Pitch and roll will be controlled by the horizontal elevons, and yaw will be controlled using differential thrust from the motors. Disturbances will be applied with schedule all-movable horizontal tail deflections supplemented by ailerons on the dihedral outer-wing sections. Those disturbances will excite wing deformation during flight, and the response will be recorded from a series of on-board sensors. Those sensors are a collection of Inertial Measurement Unit (IMU), strain gages, and accelerometers.

Five fairings are suspended at the joint of the six inboard sections. The four outboard fairings are modular (i.e., outfitted with identical hardware and electronics). Each contains a Diamond Systems PC104

Table 1 X-HALE key parameters

Parameter	Value	Unit
Wing span	8	m
Chord	0.2	m
Planform area	1.6	m^2
Aspect ratio	40	--
Length	0.96	m
Propeller diameter	0.30	m
Max payload	7.2	kg
Max gross takeoff weight	11.1	kg
Power/weight	25.5	W/kg
Airspeed	10–19	m/s
Endurance	45	min

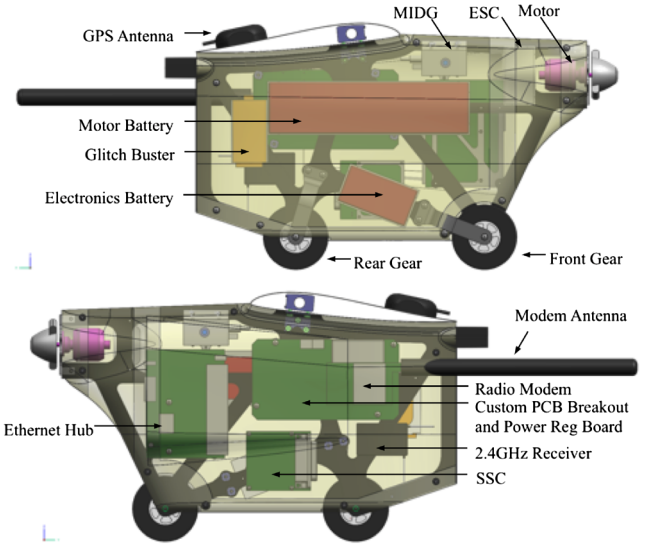

Fig. 4 Central fairing assembly.

stack of an Athena II and DMM I/O expansion cards for analog-to-digital conversion and data acquisition. The four outboard fairings also independently control elevons for pitch authority. The central fairing houses the ground station communication system and a Microbotics MIDG GPS/INS reference system. Additionally, the central fairing controls all Radio-Control (RC) command conditioning, onboard mixing, and autopilot-mode control using a Microbotics Servo Switch/Controller (SSC). Each fairing is powered with two lithium polymer batteries: an 11.1 V/1320 mAh electronics battery and an 11.1 V/6000 mAh motor battery to power each of the 18-W electric outrunner motors. The outboard motors are capable of differential control to enable vehicle yaw. This overall layout and the primary components within each fairing type are displayed in Figs. 4 and 5.

Components within each fairing are mounted to a central graphite/epoxy spine. The spine itself is connected to the wing box through custom aluminum L brackets and a joiner located within the wing box of each wing section. This transfers all loads from the fairing through the connection to the wing box only. Finally, the internal components are protected by glass/epoxy skins that are also mounted to the main spine through standoffs and recessed screws. Ram-air intakes designed into the skins profile cool both the motor and primary electronics such as the Athena II computer and power regulation circuitry during flight. The rear-flared portion of the skin is

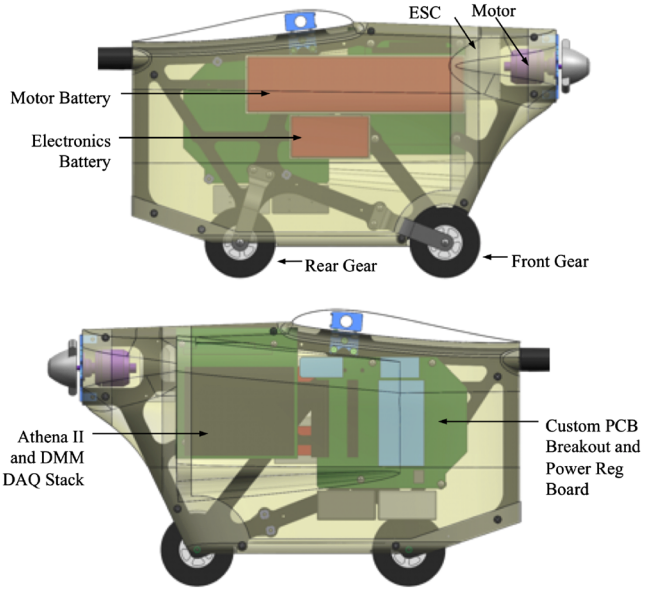

Fig. 5 Outboard fairing assembly.

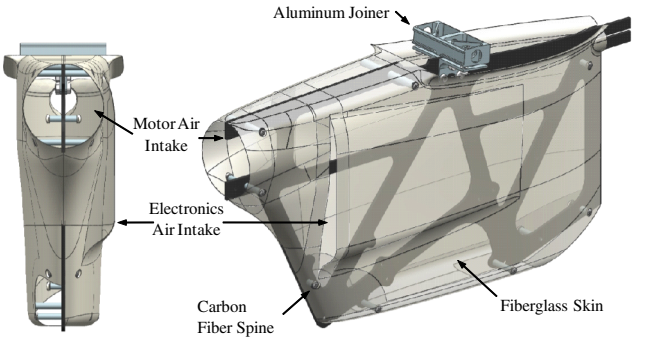

Fig. 6 Fairing structure.

also left open to provide an exit vent for the heated air. The skin is identical for each fairing, whereas the central spine is unique to common outboard fairings. The assembly of the internal fairing structure, skin, and wing joiner is displayed in Fig. 6.

B. Airfoil Selection and Characteristics

The X-HALE design was originally inspired by the Aerovironment's Helios. As a result, the original airframe was a flying wing, which led to reflex-type airfoils. Trading C_{m0}, stall angle, and L/D, the final choice was to use the EMX07 reflexed airfoil, displayed with its pressure profile in Fig. 7. Once the design progressed, horizontal tails became alternatives to placing control surfaces within the uniform wing structure. NACA 0012 airfoils were chosen because of the standard behavior of the symmetric airfoil.

With a chord of 0.2 and 0.12 m, respectively, the wing and tail Reynolds numbers are low, ranging from 150,000 to 93,000 at a 14 m/s reference cruise velocity. This has an effect on the aerodynamic derivatives of each airfoil, but it is much more significant for the NACA 0012. Figures 8 and 9 display the basic aerodynamic coefficients for each airfoil at the operating Reynolds number (150,000). Along with those, results for a high Reynolds number of 1,500,000 are included just for comparison. The results displayed in Figs. 8 and 9 show how important it is to provide custom aerodynamic data to design and/or analysis codes to produce realistic simulation results. Standard aerodynamic derivatives such as 2π for $c_{l\alpha}$ are no longer valid, especially for the NACA 0012, which ranges from 4.4 to 12 depending on the angle of attack. This dependence on the angle of attack is translated into our UM/NAST simulations through look-up tables and calibration functions to produce the most realistic simulation results. Tables 2 and 3 display the resulting aerodynamic derivatives for both airfoils. All of these data were calculated using XFOIL. Two-dimensional wind-tunnel tests are underway to verify the validity of these properties for the as-manufactured wing and tail sections.

C. Wing Design and Fabrication**

Because of the high wing flexibility, multiple design requirements for the wing structure are needed. These include (1) predictable and controlled cross-sectional properties, (2) the use of lightweight and flexible but strong materials, (3) the ability to disassemble the vehicle for transportation and ease of manufacturing, and (4) the structural behavior of a uniform beam despite a modular design. As a result, both materials and manufacturing processes are selected and prototyped to satisfy these criteria.

Prepreg composites are used as the primary structural material because of their lightweight, controlled, and documented material properties. The main wing structure is composed of a wing box made from Hexcel E-glass 120/F155 prepreg fabric wrapped around a Rohacell 31-IG high-temperature foam core. The wing box includes five continuous layers of E-glass in a 0/90 orientation to provide a robust thickness to the structure. To finish the airfoil profile,

**What follows only the wing is described, but a similar manufacturing procedure is used for the horizontal tails.

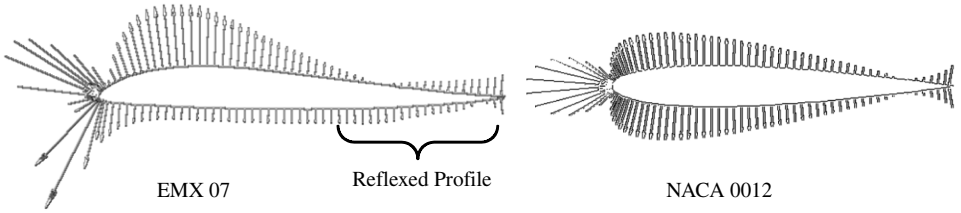

Fig. 7 Wing and tail airfoil profiles.

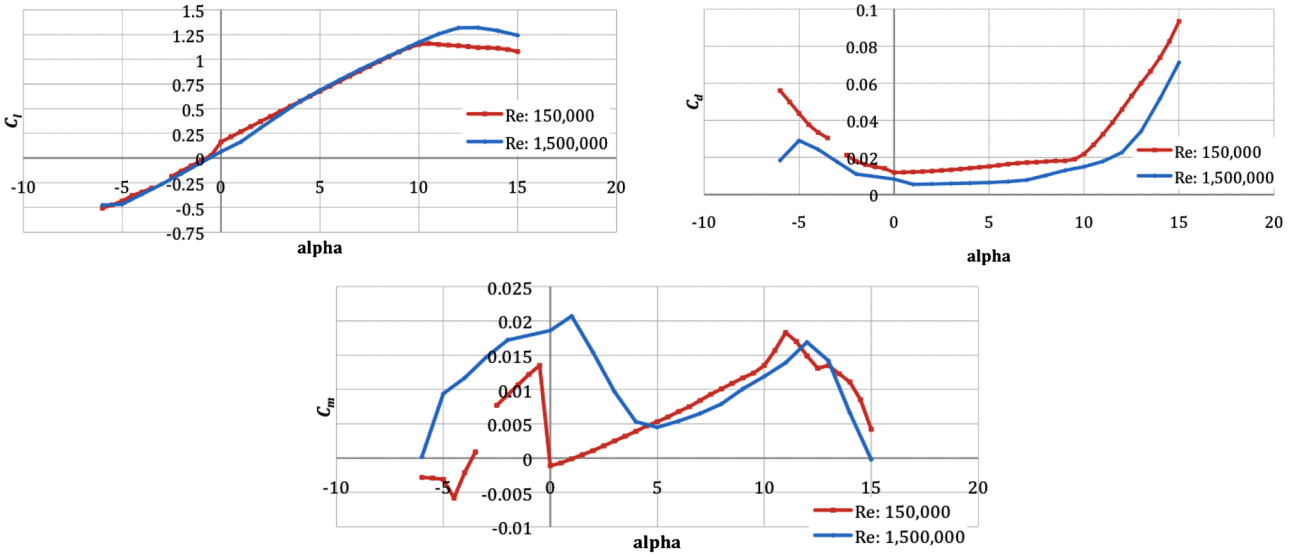

Fig. 8 EMX07 airfoil to be used in the main wing (results obtained using XFOIL).

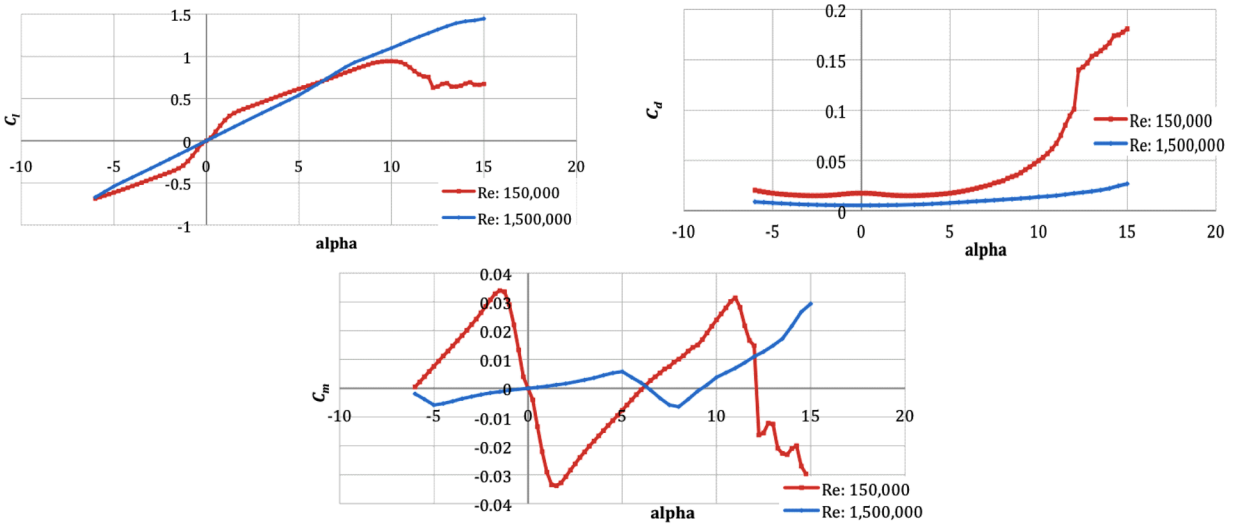

Fig. 9 NACA 0012 airfoil to be used in the horizontal tail (results obtained using XFOIL).

Table 2 EMX07 aerodynamic derivatives @ $Re = 150{,}000$

EMX07	c_l	c_d	c_m
Range (AOA)		< -0.5	
$dc_x/d\alpha$	5.8034	−0.4260	0.1641
c_{x0}	0.0717	0.0065	0.0150
Range (AOA)		(−0.5 to 10)	
$dc_x/d\alpha$	5.8034	0.0402	0.0815
c_{x0}	0.1630	0.0119	−0.0011
Range (AOA)		>10	
$dc_x/d\alpha$	−0.2521	0.7739	−0.2020
c_{x0}	1.1944	−0.1162	0.0572

additional foam is added to the leading and trailing edges and then wrapped with a final layer of 0/90 E-glass. This layup composes the majority of the wing, which can be visualized in Section B-B and Detail D of Fig. 10. Still, 3.18 cm (3.18%) from either end of the wing section contain a different layup. This layup includes layers of $IM7/977-3$ graphite/epoxy unidirectional tape to reinforce and complete the internal geometry of the wing joint, which is shown in Section A-A and Detail C and will be described later. Further details on the layup can be found in Table 4.

Because the layup in section A-A only takes up roughly 3% of the total wing mass, it is not accounted for in the simulation input that will be detailed later in Sec. III. The purpose of it in our physical model is to create a robust wing joint layup that can withstand inertial and landing loads from the fairings.

Meticulous attention has also been given to the fabrication and flight hardware used at each joint. The joint is designed to transfer

Table 3 NACA 0012 aerodynamic derivatives @ $Re = 150{,}000$

NACA 0012	c_l	c_d	c_m
Range (AOA)	0–1.5		0–1.5
$dc_x/d\alpha$	12.0145		−1.2930
c_{x0}	0.0000		0.0000
Range (AOA)	1.5–10	0 to 10	1.5–10
$dc_x/d\alpha$	4.4746		0.4119
c_{x0}	0.2240	0.0160	−0.0435
A		32.400	
B		−1.306	
C		−0.024	
Range (AOA)		>10	
$dc_x/d\alpha$	0.0000	1.6085	−0.8318
c_{x0}	0.6000	−0.2359	0.1850

bending loads through the wing box and torsional loads through the shear skin. Therefore, it must be made with tight tolerances to ensure a uniform load transfer. With this is mind, the inspiration for the current wing box joint hardware is simplicity, as it is composed of a single machined aluminum component (Fig. 11). Within this single piece of hardware, we have the ability to join both wing sections, fasten the fairing structure, and route any internal wing wiring without hindering the ability to remove or replace any single primary component. Furthermore, the joiner is machined to match the profile of the aluminum mold insert used to layup and align the internal wing-box geometry.

To help with the transfer of the torsional loads, a fiberglass sleeve is used that slides around the wing joint (Fig. 12). The airfoil profile at the end of each wing section is slightly offset, allowing the sleeve to provide a smooth transition for the airfoil surface across the joint. The use of machined components and molds within each joint component is critical for guaranteeing a rigid and straight connection across the wing span, thus satisfying the previously discussed fourth wing-design criterion.

Exceptional care has been taken in the creation of the tools necessary for manufacturing identical wing sections. Robust aluminum female molds have been machined in-house on a Computer Numerical Control (CNC) bed mill and sanded to a mirror finish to both produce the most accurate airfoil profile and the smoothest surface finish possible. The use of female molds has another benefit: it allows the foam core to be oversized and compressed by the mold surface when closed, which helps bond strain gages to the internal fiberglass surface and aides in a smooth surface finish.

Two curing cycles are required to create one full wing section. First, the wing box is fabricated. As previously described, layers of E

Table 4 Composite layup legend for detail C and D

Label	Plies	Material	Thickness, mm	Orientation[a]
1	5	E-Glass 120/F155	0.12	90,90,90,90,90
2	n/a	IM7/977-3 Dowel	1. (diameter)	0
3	5	E-Glass 120/F155	0.12	0,0,0,0,0
4	2	IM7/977-3 Tape	0.137	0,0
5	1	E-Glass 120/F155	0.12	0
6	5	E-Glass 120/F155	0.12	0,0,0,0,0
7	1	E-Glass 120/F155	0.12	0

[a]0 is along wing span.

glass are wrapped around foam sections shaped to the wing-box profile and the carbon fiber that makes up each wing joint, which has already been wrapped around plugs that attach to alignment jigs. The alignment jigs then slide onto pins embedded in the wing mold. At this point, the mold will only apply pressure to the top and bottom surfaces because the airfoil profile is incomplete. Thus, solid epoxy leading- and trailing-edge forms, referred to as hardbacks, are placed in the mold to apply pressure to the front and back of the wing box. Once the wing box has completed a curing cycle, foam leading- and

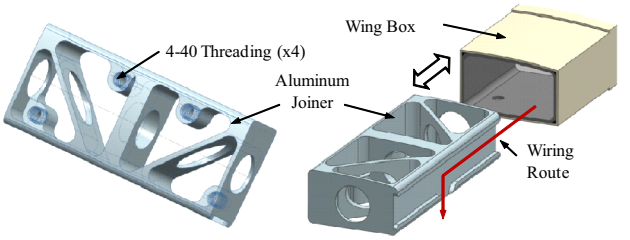

Fig. 11 Aluminum joiner and wing box assembly.

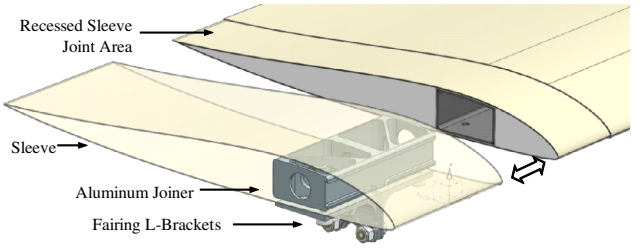

Fig. 12 Wing joint composition.

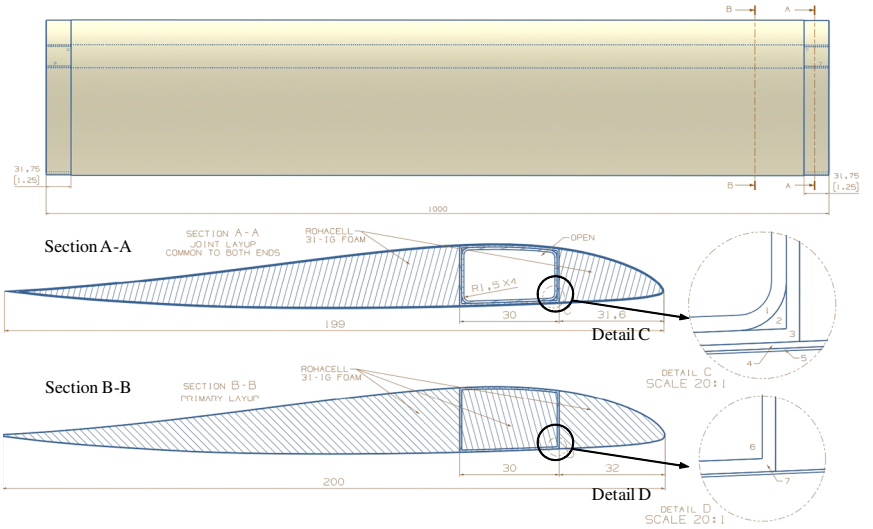

Fig. 10 Primary wing layup cross section.

Table 5 Sensors and their positioning on the planform

Board/Sensor	Color	Number	Channels	Type
DMM32 I/O PC104 card		**4**	**64 (Avail)**	
Bending strain gage bridge		26	26	Differential
Shear strain gage bridge		22	22	
In-plane strain gage bridge		16	16	
Athena II board		**4**	**64 (Avail)**	
2-axis accelerometer		12	24	Single-ended
1-axis accelerometer		8	8	
5-hole probe		3	9	
Tail potentiometer		4	4	
Fairing housekeeping				
Voltage divider circuit		10	10	
Motor rpm		5	5	
Thermocouple[a]		4	4	

[a]Not included in central fairing.

trail-edge sections replace the hardbacks, and the entire assembly is wrapped with a single layer of E-glass, with an additional layer of graphite/epoxy at the wing joints. The wing is again cured in an autoclave, producing one complete wing.

D. Sensor Layout and Design

A sizeable data acquisition network must be used to monitor X-HALE's complex aeroelastic behavior during flight. X-HALE is equipped with four Athena II single-board computers. Each has a 500-MHz processor, 256 MB of RAM, and a 1-GB flash card to process and store collected analog data. Each Athena II has a 16 single-ended analog-to-digital conversion (ADC) circuit, which is supplemented with 16 additional differential ports from a stacked Diamond-MM-32 PC/104 board I/O expansion card. The airframe is equipped to carry four of those pairs (Fig. 13), one in each outboard fairing.

Each board is designated to collect data from specific types of sensors at different rates. The sensors on board the X-HALE are categorized into two groups: science and housekeeping. Science data include all strain gages and accelerometers used in sole support to the aeroelastic tests. Housekeeping data include sensors that monitor the health of the aircraft, such as temperature and battery voltage; flight conditions (e.g., airspeed, angle of attack, side-slip angle, Euler angles, GPS location); and control inputs (e.g., motor RPM, control-surface deflections). The DMM card is tasked with sampling only the strain-gage data at 1 kHz. The Athena Data Acquisition (DAQ) circuit samples the accelerometers and housekeeping sensors at lower rates, which are adjustable by the user. Figure 14 and Table 5 describe the positioning of each sensor and their relative DAQ systems.

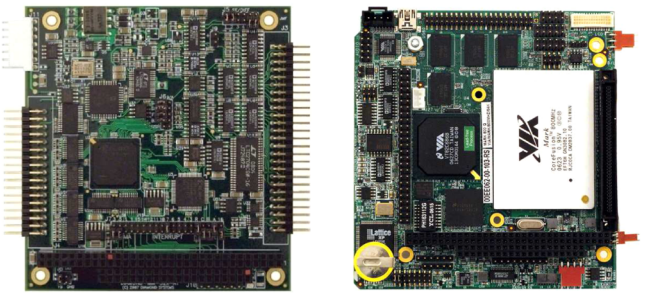

Fig. 13 Diamond systems DMM32 I/O PC104 card and Athena II single-board computer.

With 128 possible sensors, it is important that the data are time synchronized. To do this and compile the data from all fairings, the stack in Fairing 1 is programmed as a master, whereas the others are programmed as slaves. The master triggers data collection through a digital pulse. Once this occurs, each stack independently samples all science and housekeeping sensors. High-speed science data is stored locally on each Athena II, whereas the housekeeping data is sent to the master via an onboard Ethernet network. The master then stores the data and sends it to a radio modem located in the central fairing to a ground station monitored during flight. To ensure that a reliable 1-kHz data acquisition rate is possible, the QNX real-time operating system is used, and analog data are stored in a high-speed RAM queue capable of supporting more than 30 min of continuously acquired data. The ground station operator can specify when to start and stop data acquisition cycles; when active acquisition is inactive, data previously stored are then written to permanent storage, halting either when writing is complete or when the operator restarts data acquisition.

E. Flight-Control System

During the majority of the flight, X-HALE is completely under RC command, with manual servo commands monitored and stored onboard. It is only during cruise condition that predetermined motor and control surface commands are issued by the onboard master flight computer. In early testing, open-loop (scripted) command sequences designed to appropriately excite aeroelastic behaviors will be the only autopilot control capability. Based on analyses from this

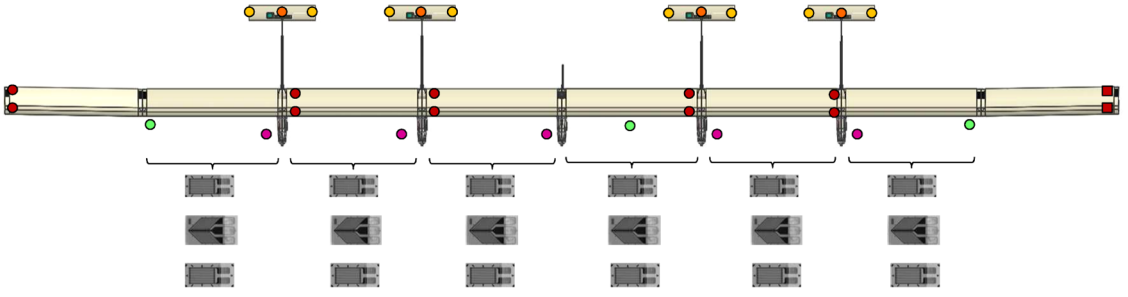

Fig. 14 General sensor layout on X-HALE planform view.

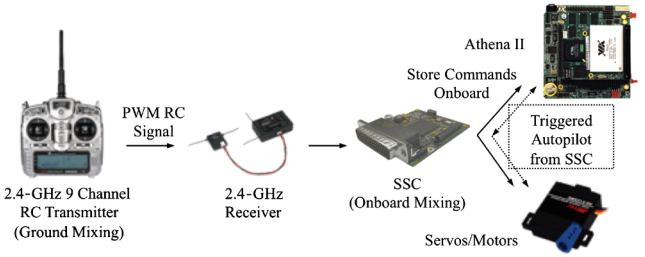

Fig. 15 Functional diagram of the RC command mixing sequence.

testing, we will then migrate to a feedback control strategy appropriate for the very flexible body.

The X-HALE has nine RC components composed of five motors and four tails. Ailerons are also included on each of the dihedral wing sections, but they will only be used during testing phases of the flight to force deformations into the wing structure. Mixing both on the ground through the RC transmitter and onboard through the SSC allows the pilot to control each RC component through the standard four-channel thrust, yaw, pitch, and roll joysticks on the transmitter, or to trigger the autopilot phase through an additional channel such as a gear or flap switch. All commands are stored onboard and also sent to the ground station. To supplement the Pulse width modulation (PWM) commands, sensors monitor the physical motion of each control component to alleviate any errors in the conversion to mechanical energy. Figure 15 displays a functional graphical diagram of the mixing phases of the RC signals.

Specific mixing percentages will be determined on the benchtop and refined between early flight tests, but the strategy for control mixing will be as follows. Thrust (throttle joystick) will ramp from 0 to 100% equally over all motors to balance battery use given the zero-yaw (rudder joystick) command. With the need to apply a yawing moment, the two outboard motors will be issued differential thrusts that, within saturation limits, apply the appropriate moment while maintaining the desired total thrust. Similarly, the horizontal tail surfaces will be uniformly deflected in response to elevator commands, with the two outboard tails adjusted in opposite directions to obtain any desired roll moment (commanded with the aileron stick on the transmitter).

Each outboard fairing has an all-movable tail. The Hitec 5125 digital slim wing servo used for actuation and the circuitry used to record the position of the tail are embedded within the NACA 0012 airfoil profile along the tail axel. With this arrangement, the axel is

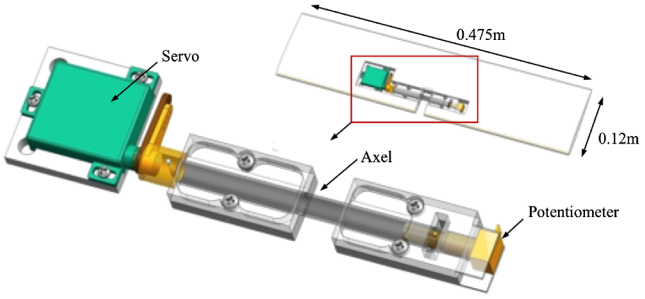

Fig. 16 Tail and internal hardware.

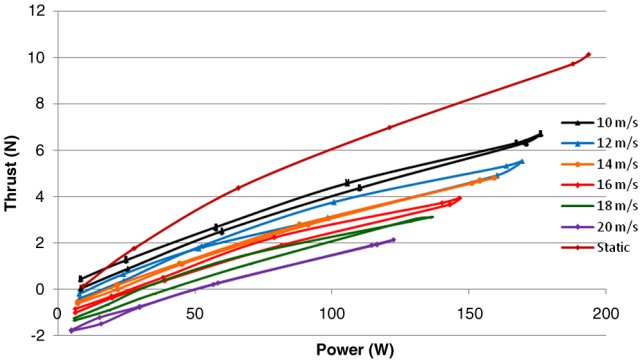

Fig. 18 Input power vs. thrust from wind-tunnel testing for flight-regime velocities.

fixed to the boom while the tail rotates around it. The physical angular position of the tail is measured by the change in resistance from a rotary potentiometer to provide a direct measurement of the PWM signal that is sent to the servo. Figure 16 displays the tail and its internal hardware.

The X-HALE is propelled by five PJS 1200 outrunner motors, each paired with a 12-by-6 Graupner CAM folding propeller. Each motor has a maximum static thrust of approximately 10 N, with a maximum power draw of 18 W. Wind-tunnel tests using a sting balance were completed to track the 6-DOF dynamic force and moment performance of the power train between 10 m/s and 20 m/s. The test setup and thrust results are displayed in Figs. 17 and 18.

Because of small inconsistencies within motor performance characteristics, each motor is tested and calibrated independently. These tests allow us to achieve and calibrate an accurate thrust profile across the span of the aircraft.

III. X-HALE Aeroelastic Simulations

A model of the X-HALE was created in UM/NAST to support its nonlinear aeroelastic analysis and design. The University of Michigan's Nonlinear Aeroelastic Simulation Toolbox (UM/NAST) integrates a low-order, strain-based geometrically nonlinear beam formulation, Peters' finite-state unsteady subsonic aerodynamic model, and flight dynamic equations to allow for the coupled aeroelastic and flight dynamic analysis of very flexible aircraft in free flight. Different nonlinear effects can be accounted for in this framework, whereas the low computational cost makes it efficient for preliminary vehicle design and control evaluation. Details about the theoretical formulation of UM/NAST can be found in [20,26]. In what follows, numerical aeroelastic and flight dynamic simulations are performed based on the model, and some fundamental aeroelastic characteristics of the model are identified. Extreme flight conditions are presented to indicate the limits in which the design can be taken.

A. Platform Data

Figure 19 illustrates the X-HALE model created in UM/NAST, which features an 8-m span. The outer 1-m-long members are built with a 10-deg dihedral angle. Five pods are modeled as vertical lifting surfaces with applied follower concentrated forces to simulate the

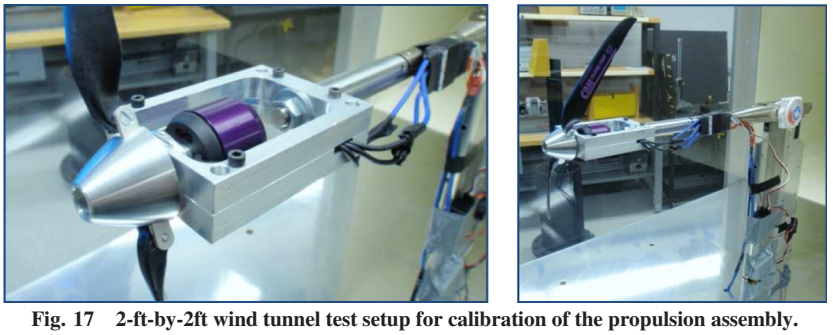

Fig. 17 2-ft-by-2ft wind tunnel test setup for calibration of the propulsion assembly.

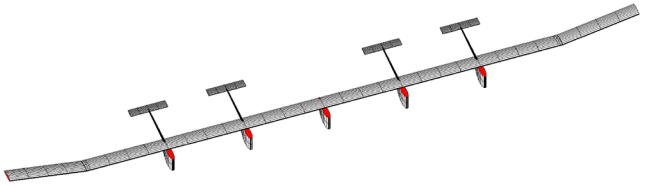

Fig. 19 UM/NAST model of the X-HALE aircraft.

motor thrust. Four tails are modeled as all-movable horizontal surfaces. Member properties are listed in Tables 6 and 7. Note that the booms, tails, and pods are modeled as rigid members, and no rigidity properties are provided for them. Ailerons are modeled on the outer dihedral members, which occupy 25% of the chord. The inertias of the spine and covers of the pods are neglected, whereas concentrated inertias are attached inside the pods, which come mainly from the electronic equipment.

B. Trim Results

The vehicle is trimmed for equal lift and weight, as well as zero pitching moment about its center of gravity, at level flight at 30-m altitude. The flight velocity ranges from 12 m/s to 20 m/s. The trim results are plotted in Fig. 20. Figure 21 compares the deformed shape at the trimmed condition (14 m/s) and the reference shape, where the large static deformation can be found. The vehicle is highly flexible and the tip deflection at this trimmed state is approximately 37% of the half span.

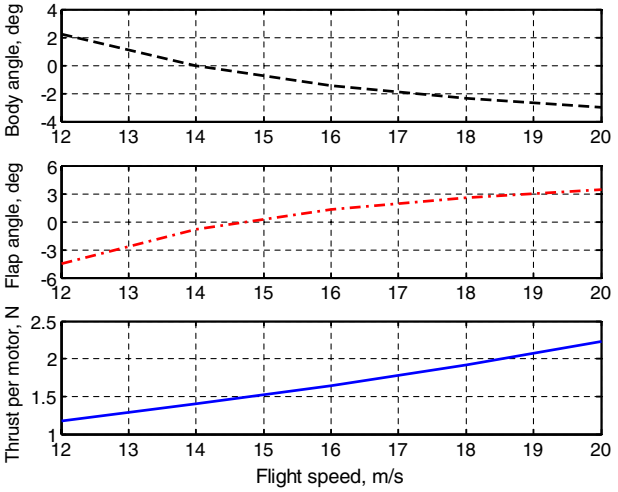

Fig. 20 Trim results of the X-HALE model.

C. Flight Under Gust Perturbations

Gust response of the vehicle is studied in this section. Figure 22 shows the 1-cosine gust profile for the simulation. The gust is symmetrically applied to the vehicle on its flight path. The maximum gust speed is 4 m/s, while the nominal flight speed is 14 m/s at 30 m altitude.

Table 6 Member properties of the X-HALE model

	Wing	Booms	Tails	Pods	Units
Ref. axis location (from L.E.)	28.78	50	32.35	60.93	% chord
Center of gravity (from L.E.)	25	50	25	25	% chord
Incidence angle	5	N/A	0	0	deg
Chord length (c)/Diameter (d)	0.20	$0.024(f)/0.013(r)$	0.11	0.37	m
Mass per unit span (m)	0.319	0.01	0.129	--	kg/m
Rotational inertia (I_{xx})	8.09×10^{-4}	2.91×10^{-9}	1.60×10^{-4}	--	kg · m
Rot./flat bend inertia (I_{xy})	0	0	0	--	kg · m
Rot./in-plane bend inertia (I_{xz})	0	0	0	--	kg · m
Flat bend inertia (I_{yy})	1.22×10^{-5}	1.46×10^{-9}	2.91×10^{-6}	--	kg · m
Flat/in-plane bend inertia (I_{yz})	-6.49×10^{-6}	0	0	--	kg · m
In-plane bend inertia (I_{zz})	7.97×10^{-4}	1.46×10^{-9}	1.57×10^{-4}	--	kg · m
Ext. stiffness (k_{11})	2.14×10^{6}	--	--	--	N
Ext./torsion stiffness (k_{12})	0	--	--	--	N
Ext./flat bend stiffness (k_{13})	1.54×10^{3}	--	--	--	N
Ext./in-plane bend stiffness (k_{14})	-4.91×10^{4}	--	--	--	N
Torsion stiffness (k_{22})	72.25	--	--	--	N · m^2
Tor./flat bend stiffness (k_{23})	0	--	--	--	N · m^2
Tor./in-plane bend stiffness (k_{24})	0	--	--	--	N · m^2
Flat bend stiffness (k_{33})	119.57	--	--	--	N · m^2
Flat/in-plane bend stiffness (k_{34})	−46.34	--	--	--	N · m^2
In-plane bend stiffness (k_{44})	6.35×10^{3}	--	--	--	N · m^2

Table 7 List of the concentrated inertias of the X-HALE model

	Outboard pods			Center pod			Inner half tail	Outer half tail	Units
	Battery forward cg	Battery aft cg	Remaining assembly	Battery forward cg	Battery aft cg	Remaining assembly			
mass	0.396	0.396	1.057	0.396	0.396	1.025	0.049	0.020	kg
x_{cg} [a]	0.013	0.013	−0.006	0.013	0.013	−0.003	0.073	0.029	m
y_{cg}	0.059	−0.001	0.066	0.059	−0.001	0.043	−0.008	0	m
z_{cg}	−0.069	−0.069	−0.085	−0.069	−0.069	−0.080	−0.001	0	m
I^c_{xx}	1.160×10^{-3}		1.134×10^{-2}	1.160×10^{-3}		1.476×10^{-2}	4.631×10^{-6}	1.866×10^{-7}	kg · m^2
I^c_{yy}	9.485×10^{-5}		3.209×10^{-3}	9.485×10^{-5}		2.816×10^{-3}	2.282×10^{-5}	1.341×10^{-6}	kg · m^2
I^c_{zz}	1.098×10^{-3}		8.484×10^{-3}	1.098×10^{-3}		2.503×10^{-4}	2.651×10^{-5}	1.311×10^{-6}	kg · m^2
I^c_{xy}	0		-1.212×10^{-3}	0		2.322×10^{-4}	-3.190×10^{-6}	1.000×10^{-10}	kg · m^2
I^c_{xz}	0		1.055×10^{-5}	0		2.267×10^{-5}	-3.057×10^{-7}	0	kg · m^2
I^c_{yz}	0		4.595×10^{-5}	0		4.500×10^{-4}	2.644×10^{-8}	0	kg · m^2

[a]The center of gravity locations are measured from the root of each member, i.e., the top surfaces for the pod members and the connection point with the boom for the tail members.

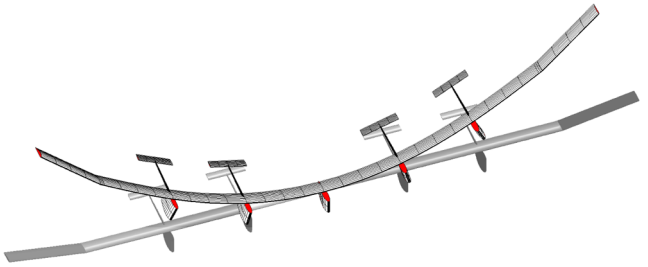

Fig. 21 Deformation at trim condition (speed: 14 m/s, with vehicle in gray as the undeformed shape).

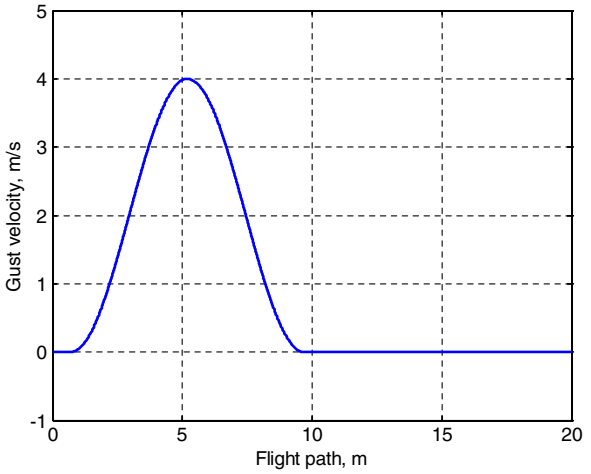

Fig. 22 Spatial-distributed gust profile.

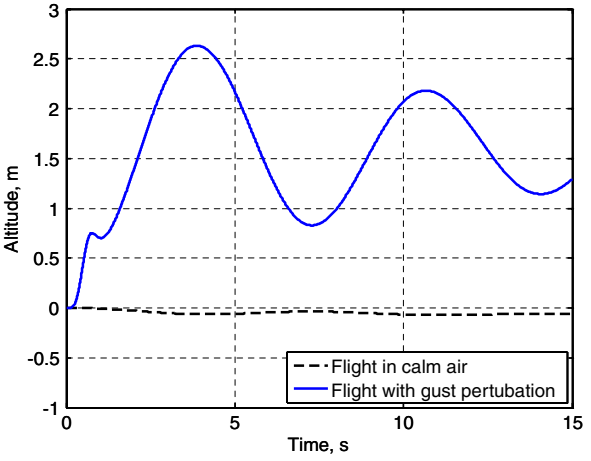

Fig. 23 Change of altitude with the gust perturbation.

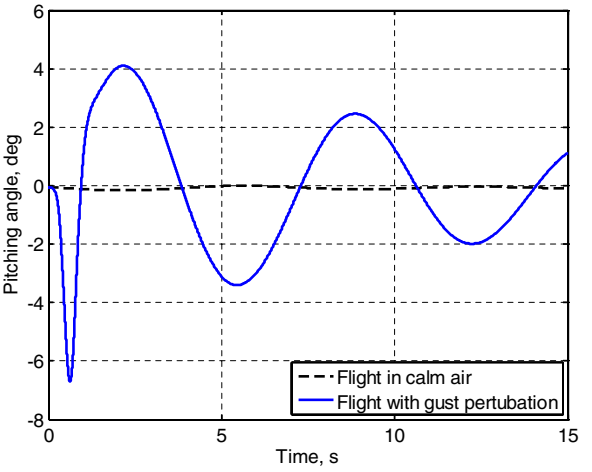

Fig. 24 Change of pitching angle with the gust perturbation.

The aeroelastic and flight dynamic responses of the model with gust perturbation are plotted in Figs. 23–27, compared to a flight condition without gust. Overall, the plunging (Fig. 23) and pitching (Fig. 24) oscillations are excited by the gust perturbation. However, the longitudinal motions are stable, as the amplitudes of the oscillations are reduced in the subsequent cycles. Figure 25 shows the velocity of the body reference frame resolved in the inertia frame. Comparing Figs. 23 and 25, one can identify the phugoid motion, which features the exchange between kinematic (longitudinal velocity) and potential energies.

Of particular interest is the flexibility of the vehicle. Figure 27 shows the wing tip deflection with the gust perturbation, normalized by the half span of the vehicle. Large wing deformations can be found to be more than 43% of the half span during the vehicle's passing the gust region, after which the oscillation in wing bending is reduced. With such large transient deformation, one must check the composite layup strains to verify the structural integrity. The maximum and minimum strain components in each composite fiber direction are shown in Table 8. The normal strain in the longitudinal direction (ε_{11}) is more than $3,000\ \mu\varepsilon$. Figure 28 plots the normal strains in the fiber's longitudinal direction, with the minima plotted as positive values. As the local strain components have already gone beyond $3000\ \mu\varepsilon$ (for a working limit of $4000\ \mu\varepsilon$), this gust profile can be considered a critical gust input of what the vehicle can sustain.

D. Vehicle Response Due to Controlled Finite Excitation

As part of the requirements for the X-HALE, the aircraft must present unstable but controlled nonlinear aeroelastic-coupled-flight-dynamics characteristics. The control surfaces present in the dihedral wing segments are not used as primary flight control surfaces, but are instead used to create disturbances to aircraft. In their anti-symmetric

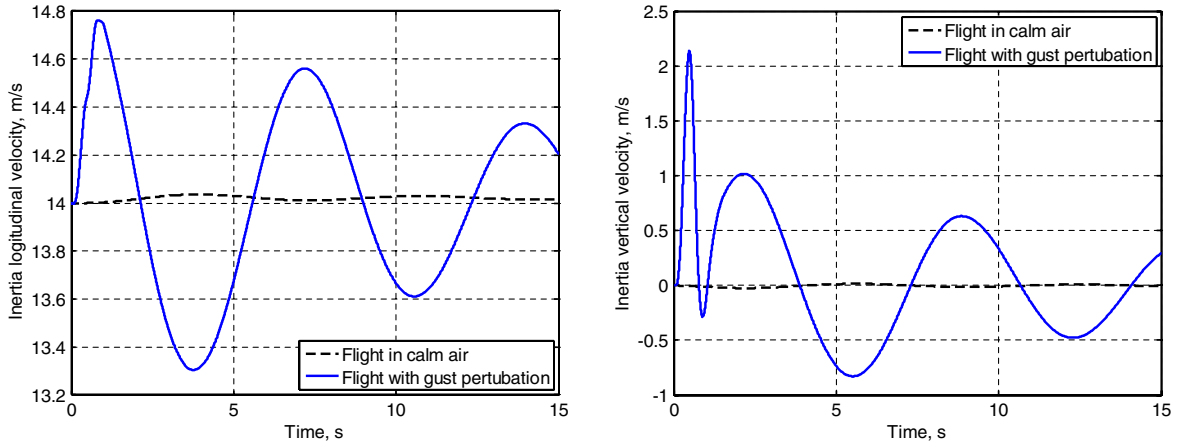

Fig. 25 Velocity components in the inertia frame.

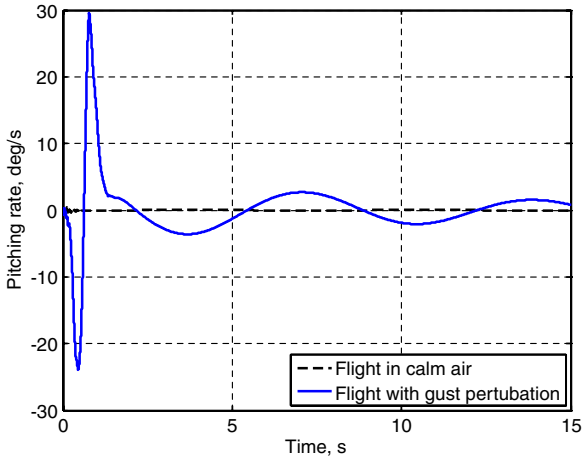

Fig. 26 Pitching rate.

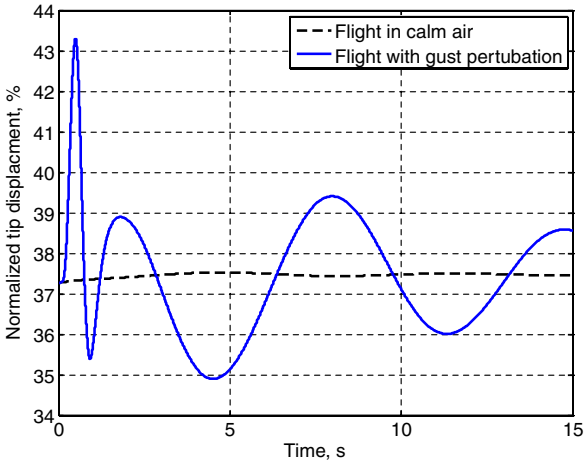

Fig. 27 Normalized tip displacement.

configuration (purely ailerons), they can excite the vehicle to a simulated anti-symmetric gust disturbance. Figure 29 exemplifies the aileron deflection angle on the left wing. The ailerons start to deflect after 5 s (into the simulation) and complete one sinusoidal cycle within 2 s. As indicated in Fig. 29, two simulations are performed to study the roll characteristic of the X-HALE model. One has the maximum aileron deflection of 2 deg (representing a small disturbance), while the other has the maximum aileron deflection of 5 deg (representing a large disturbance).

First, roll angles and roll rates are compared for the two simulations in Figs. 30 and 31. According to the aileron input, the vehicle is commanded to roll in its positive direction (i.e., right wing down). From the numerical simulation, one might find the vehicle slightly rolls negatively immediately after the aileron input, which is easier to see in the plot of roll rate (Fig. 31). Right after that, the vehicle rolls back to its positive direction. This positive roll does not hold for a long time before the vehicle starts to develop another negative roll due to the evolution of the commanded aileron deflections. After the one-cycle actuation, the oscillation in roll is developed. Figure 30 shows that the roll motion with 5-deg actuation is not stable because the magnitude of the roll angle is increased, whereas the roll after 2-deg actuation is still stable.

To verify if the instability in roll after the 5-deg actuation is purely rigid-body instability or is due to the coupling between the flexible and rigid-body degrees of freedom, one more simulation is carried out in which the wing flexibility is neglected. The vehicle is first brought to its nonlinear trimmed state, and then the wing deformation is locked in place. Only rigid-body degrees of freedom are considered for that. Figures 32 and 33 compare the results from this simulation with the ones from fully nonlinear simulation above. The rigid-body simulation predicts a stable roll motion. Therefore, the

Table 8 Maximum and minimum strains with the gust perturbation

	Maximum ($\mu\varepsilon$)	Minimum ($\mu\varepsilon$)
ε_{11}	3093.4	−3656.0
ε_{12}	895.8	−886.8
ε_{13}	1079.8	−1068.9
ε_{22}	1241.3	−1099.8
ε_{23}	773.0	−778.1
ε_{33}	769.2	−569.9

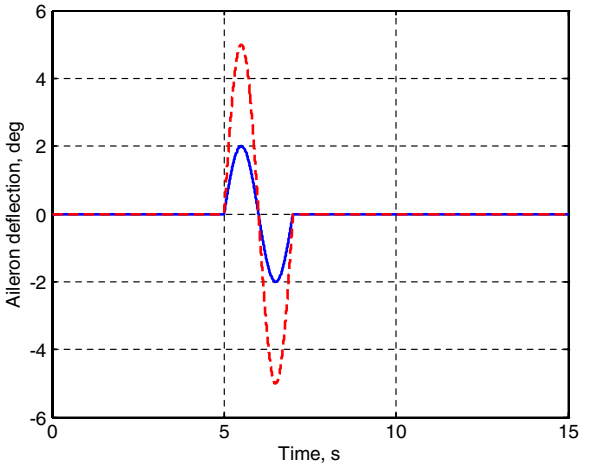

Fig. 29 Aileron deflection on the left wing.

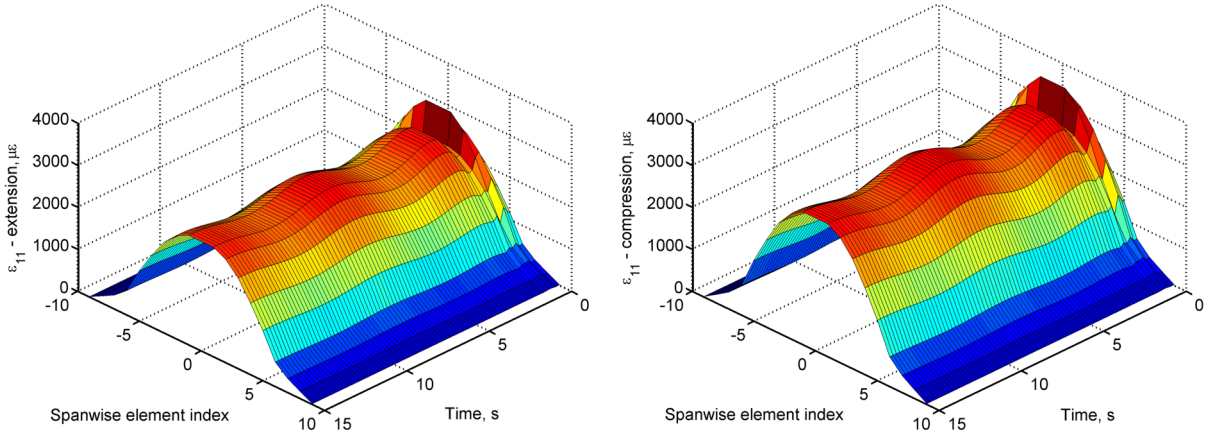

Fig. 28 Normal strains in fiber longitudinal direction ε_{11}. Left: extension. Right: compression.

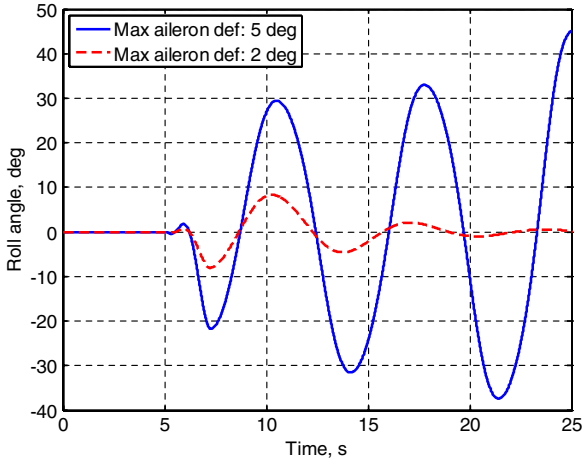

Fig. 30 Change in the roll angle of the vehicle with different aileron inputs.

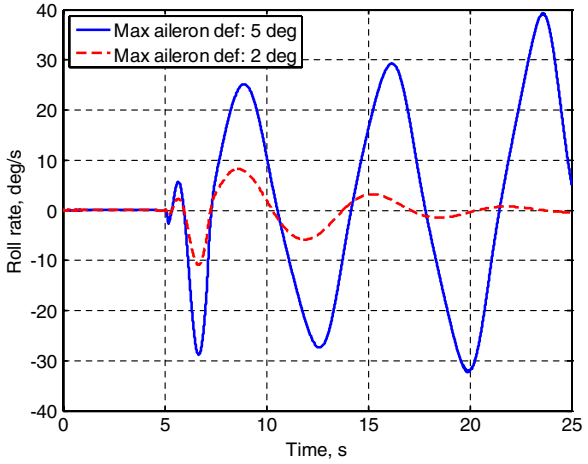

Fig. 31 Change in the roll rate of the vehicle with different aileron inputs.

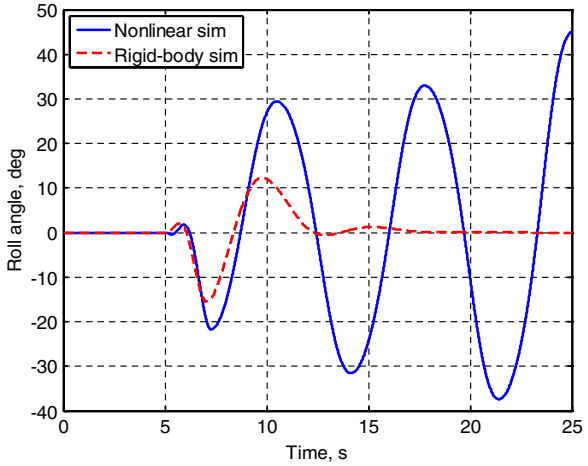

Fig. 32 Roll angle from different simulations.

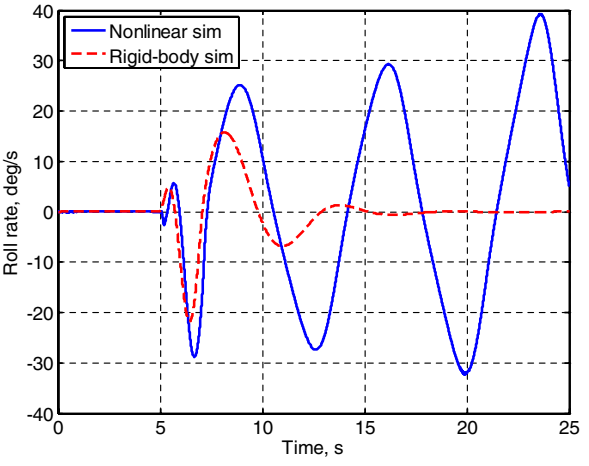

Fig. 33 Roll rate from different simulations.

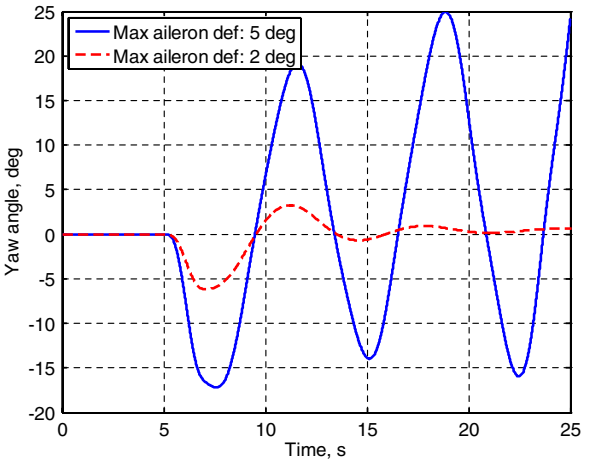

Fig. 34 Change in the yaw angle of the vehicle with different aileron inputs.

instability observed from the fully nonlinear simulation is a true coupled, nonlinear aeroelastic and flight dynamics one as desired for this experiment. Further investigation of the vehicle response and deformation shows that the unstable mode is a Dutch-roll coupled with the first wing bending mode.

Significant yaw moment to the vehicle is introduced by the aileron disturbances. Oscillations in yaw can be observed in Fig. 34. Moreover, pitching oscillations are also excited (Fig. 35), and the simulation indicates that the larger disturbance (5-deg aileron deflection) may lead to instability after several cycles. This may be simply a numerical issue, and the flight test will verify it. If this pitch instability happens during flight tests, corrective actions must be taken by the pilot to arrest it. Finally, oscillations of the vehicle's body reference frame in the lateral and vertical directions also occur as expected as shown in Figs. 36 and 37.

Figure 38 shows the wing tip deflections due to the aileron input. The additional wing tip deflection due to a 2-deg aileron input is

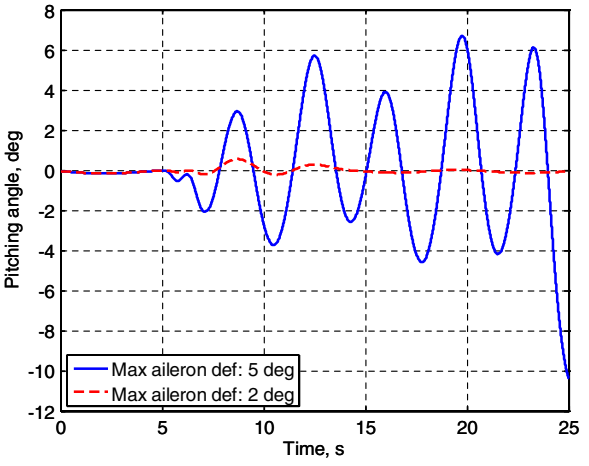

Fig. 35 Change in the pitching angle of the vehicle with different aileron inputs.

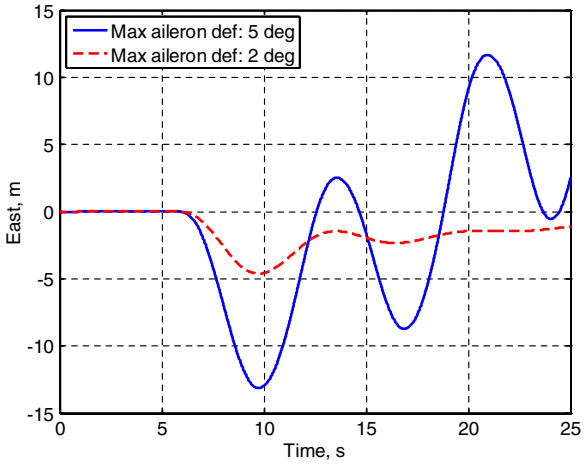

Fig. 36 Change in the lateral position of the vehicle with different aileron inputs.

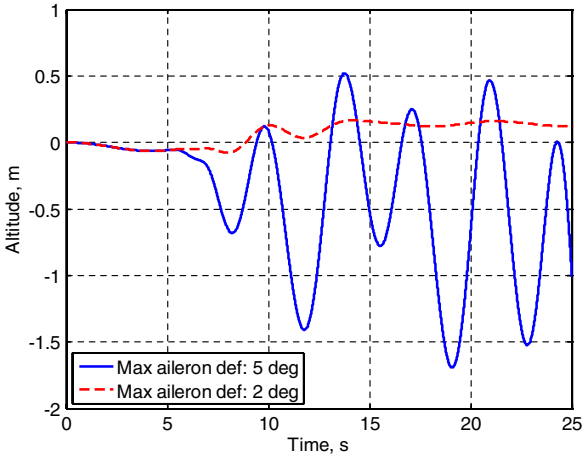

Fig. 37 Change in the altitude of the vehicle with different aileron inputs.

relatively small when compared with the state at initial level flight. The magnitude of the bending oscillation is reduced with time, and the wing deformation is recovering to the steady state. For the simulation with 5-deg aileron input, however, the wing deformation introduced by the aileron deflection is significantly larger, where the right wing tip deflection can exceed 42% of the half span. It is also clear that the bending oscillation of the wing is increased after the aileron actuation. Therefore, the 5-deg aileron input case (under this frequency of 0.5 Hz) can be seen as an upper limit for excitation

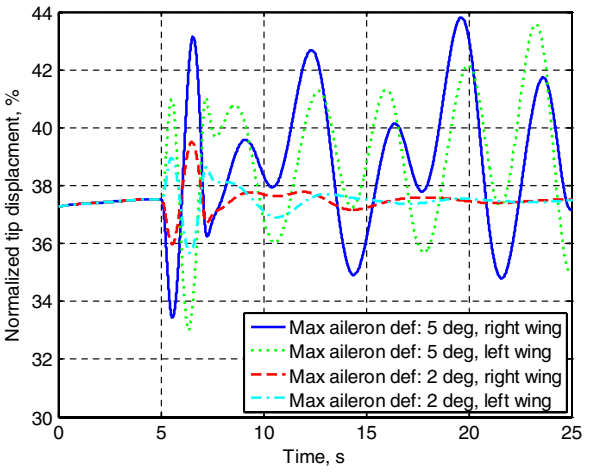

Fig. 38 Normalized wing-tip deflections.

Table 9 Maximum and minimum strains with the 5-deg aileron inputs

	Maximum ($\mu\varepsilon$)	Minimum ($\mu\varepsilon$)
ε_{11}	2881.0	−3,499.2
ε_{12}	587.9	−478.4
ε_{13}	708.7	−576.7
ε_{22}	1182.0	−1024.5
ε_{23}	758.8	−756.8
ε_{33}	752.7	−516.5

during flight. In this model, the aileron was taken as a full-section span (1-m long), but in the actual X-HALE, it would be a span of no more than 25 cm. This will allow for an equivalent 20-deg aileron input for similar vehicle response. Limits on the aileron deflections will be provided by software.

Table 9 lists the strain components in the material direction. Again, one can see the normal strain in the longitudinal direction exceeds 3000 $\mu\varepsilon$. Figure 39 plots the span wise and spatial distributions of the strain in this direction. The large strain happens after the aileron actuation.

IV. Conclusions

This paper introduced the X-HALE remotely piloted aircraft as a test bed for nonlinear aeroelastic flight tests. The 8-m-span, very flexible aircraft is expected to excite nonlinear aeroelastic and flight dynamic coupled responses due to controlled excitation that will provide valuable data in support of code validation. The design and manufacturing processes chosen for the airframe are such that the

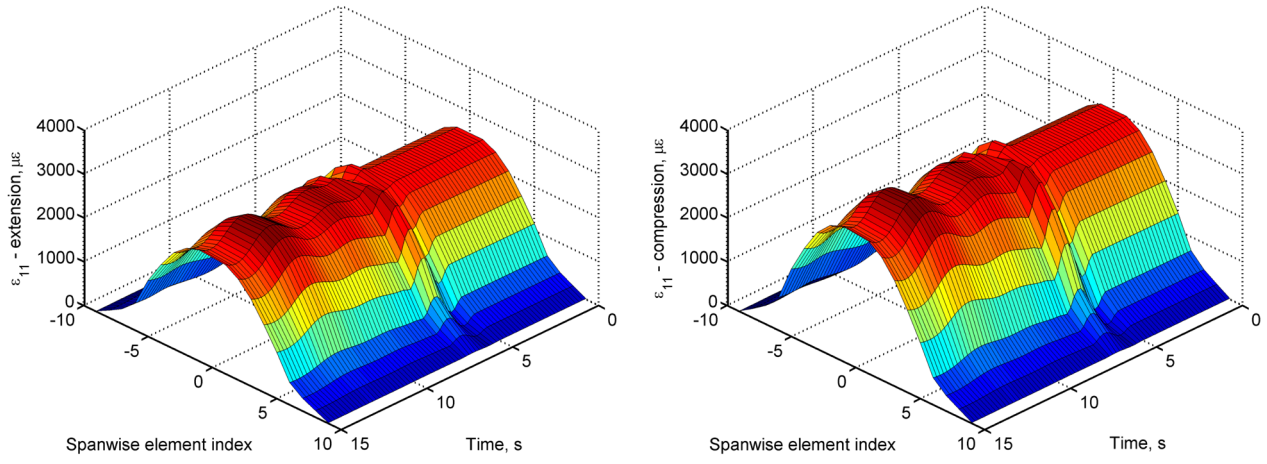

Fig. 39 Normal strains in fiber longitudinal direction (ε_{11}, left: extension; right, compression).

elastic, inertial, and geometric properties can be well characterized. The integrated airframe, on-board computers, controls, and software were presented. A network of strain gages and accelerometers provides measurements for the instantaneous deflection shape. Three 5-hole probes along the wingspan provide basic aerodynamic data. Engine thrust (through rpm measurement), control surface rotations, and center-pod inertial measurements are also obtained during flight. Batteries provide power to the five electric motors for flights lasting up to 45 min, which will be enough to conduct several test points. Manufacturing of the first flight-test vehicle is underway, along with a series of bench tests to fully characterize various structures, aerodynamics, propulsion, electronics, and software-unique aspects of the X-HALE.

The expected X-HALE aeroelastic behavior was obtained using UM/NAST, a comprehensive preliminary aeroelastic design tool for very flexible aircraft. The design presents significant wing deflections under trimmed conditions as desired. It also has the control authority to excite large dynamic responses and to even develop (controlled) aeroelastic instabilities. Because of the large deformation under trimmed conditions, the safety margins left for the vehicle to sustain gust perturbations and maneuver must be closely monitored, as the local normal strains could transiently exceed 3000 $\mu\varepsilon$. From the simulation with anti-symmetric large aileron disturbances, the aircraft can develop an unstable Dutch-roll coupled with first wing bending modes. Moreover, complex 3-D rotational and translational motions were observed with the large aileron input, which indicate a desirable test point to be explored during flight tests and for which wind tunnel tests would not be feasible.

The goal for the first phase of flight tests is to assess the X-HALE handling qualities, its basic aeroelastic response, and how these correlate with UM/NAST predictions. From those, small design adjustments are expected, and a new airframe will be finalized for the aeroelastic flight tests.

Acknowledgments

This work has been supported in part by the Air Force Research Laboratory under the Michigan/AFRL Collaborative Center in Aeronautical Sciences (MACCAS). The technical monitors were Edward Alyanak, Gregory Brooks, and Nathan Pitcher [Air Force Research Laboratory (AFRL)/RBAA]. Additional funds were also provided by the University of Michigan's Active Aeroelasticity and Structures Research Laboratory. Finally, the authors would like to thank the University of Michigan students who have supported the X-HALE development: Roy Blankman, Blake Davis, Daniel Ellis, Marc Lecerf, Kevin Gregus, Elizabeth Prentice, and Jonathan Wiebenga.

References

[1] Tilmann, C. P., Flick, P. M., Martin, C. A., and Love, M. H., "High-Altitude Long Endurance Technologies for SensorCraft," MP-104-P-26, *RTO AVT-099 Symposium on Novel and Emerging Vehicle and Vehicle Technology Concepts*, 2003, Brussels, Belgium.

[2] Whitson, S., "The Proteus, Giving Shape to Forms Unknown," *Private Pilot*, Vol. 33, No. 12, 1998, pp. 44–50.

[3] Palacios, R., Cesnik, C. E. S., and Reichenbach, E., "A Re-Examination of the Structural Design Procedures for Very Flexible Aircraft," *International Forum on Aeroelasticity and Structural Dynamics 2007*, Stockholm, Sweden, 18–21 June 2007.

[4] Shearer, C. M., and Cesnik, C. E. S., "Nonlinear Flight Dynamics of Very Flexible Aircraft," *Journal of Aircraft*, Vol. 44, No. 5, 2007, pp. 1528–1545. doi:10.2514/1.27606

[5] Wilson, J. R., "Fly Like a Vulture," *Aerospace America*, Vol. 46, No. 11, 2008, pp. 28–33.

[6] Noll, T. E., Brown, J. M., Perez-Davis, M. E., Ishmael, S. D., Tiffany, G. C., and Gaier, M., "Investigation of the Helios Prototype Aircraft Mishap. Vol. 1: Mishap Report" [online article], http://www.nasa.gov/pdf/64317main_helios.pdf [retrieved 18 Dec. 2011].

[7] U.S. Army Aviation and Missile Command, RCAS User's Manual, Ver. 2.0, Moffett Field, CA.

[8] Drela, M., "Integrated Simulation Model for Preliminary Aerodynamic, Structural, and Control-Law Design of Aircraft," *40th AIAA/ASME/ASCE/AHS/ASC Structures, Structural Dynamics, and Materials Conference and Exhibit*, AIAA Paper 1999-1394, St. Louis, MO, 1999.

[9] Patil, M. J., Hodges, D. H., and Cesnik, C. E. S., "Nonlinear Aeroelasticity and Flight Dynamics of High-Altitude Long-Endurance Aircraft," *Journal of Aircraft*, Vol. 38, No. 1, 2001, pp. 88–94. doi:10.2514/2.2738

[10] Cesnik, C. E. S., and Brown, E. L., "Modeling of High Aspect Ratio Active Flexible Wings for Roll Control," *43rd AIAA/ASME /ASCE/AHS/ASC Structures, Structural Dynamics, and Materials Conference*, AIAA Paper 2002-1719, Denver, CO, 2002.

[11] Cesnik, C. E. S., and Su, W., "Nonlinear Aeroelastic Modeling and Analysis of Fully Flexible Aircraft," *46th AIAA/ASME/ASCE/AHS/ASC Structures, Structural Dynamics, and Materials Conference*, AIAA Paper 2005-2169, Austin, TX, 2005.

[12] Patil, M. J., and Hodges, D. H., "Flight Dynamics of Highly Flexible Flying Wings," *Journal of Aircraft*, Vol. 43, No. 6, 2006, pp. 1790–1798. doi:10.2514/1.17640

[13] Shearer, C. M., and Cesnik, C. E. S., "Trajectory Control for Very Flexible Aircraft," *Journal of Guidance, Control, and Dynamics*, Vol. 31, No. 2, 2008, pp. 340–357. doi:10.2514/1.29335

[14] Chang, C.-S., Hodges, D. H., and Patil, M. J., "Flight Dynamics of Highly Flexible Aircraft," *Journal of Aircraft*, Vol. 45, No. 2, 2008, pp. 538–545. doi:10.2514/1.30890

[15] Van Schoor, M. C., and von Flotow, A. H., "Aeroelastic Characteristics of a Highly Flexible Aircraft," *Journal of Aircraft*, Vol. 27, No. 10, 1990, pp. 901–908. doi:10.2514/3.45955

[16] Jones, R. I., "Selection and Comparison of Unmanned Aircraft Configurations," A97-21501 04-01, *12th RPVs International Conference*, Bristol, U.K., 1996.

[17] Jones, R. I., "The Design Challenge of High-Altitude Long-Endurance (HALE) Unmanned Aircraft," *Aeronautical Journal*, Vol. 103, No. 1024, 1999, pp. 273–280.

[18] Cesnik, C. E. S., and Brown, E. L., "Active Wing-Warping Control of a Joined-Wing Airplane Configuration," *44th AIAA/ASME/ASCE/AHS/ASC Structures, Structural Dynamics, and Materials Conference*, AIAA Paper 2003-1715, Norfolk, VA, 2003.

[19] Cesnik, C. E. S., and Ortega-Morales, M., "Active Aeroelastic Tailoring of Slender Flexible Wings," *International Forum on Aeroelasticity and Structural Dynamics 2003*, Madrid, Spain, 2003.

[20] Su, W., and Cesnik, C. E. S., "Dynamic Response of Highly Flexible Flying Wings," *AIAA Journal*, Vol. 49, No. 2, 2011, pp. 324–339. doi:10.2514/1.J050496

[21] Minguet, P., and Dugundji, J., "Experiments and Analysis for Composite Blades Under Large Deflections, Part I: Static Behavior," *AIAA Journal*, Vol. 28, No. 9, 1990, pp. 1573–1579. doi:10.2514/3.25255

[22] Minguet, P., and Dugundji, J., "Experiments and Analysis for Composite Blades Under Large Deflections, Part II: Dynamic Behavior," *AIAA Journal*, Vol. 28, No. 9, 1990, pp. 1580–1588. doi:10.2514/3.25256

[23] Chandra, R., and Chopra, I., "Structural Response of Composite Beams and Blades with Elastic Couplings," *Composites Engineering*, Vol. 2, Nos. 5–7, 1992, pp. 347–374. doi:10.1016/0961-9526(92)90032-2

[24] Tang, D., and Dowell, E. H., "Experimental and Theoretical Study on Aeroelastic Response of High-Aspect-Ratio Wings," *AIAA Journal*, Vol. 39, No. 8, 2001, pp. 1430–1441. doi:10.2514/2.1484

[25] Tang, D., and Dowell, E. H., "Experimental and Theoretical Study of Gust Response for High-Aspect-Ratio Wing," *AIAA Journal*, Vol. 40, No. 3, 2002, pp. 419–429. doi:10.2514/2.1691

[26] Su, W., and Cesnik, C. E. S., "Nonlinear Aeroelasticity of a Very Flexible Blended-Wing-Body Aircraft," *Journal of Aircraft*, Vol. 47, No. 5, 2010, pp. 1539–1553. doi:10.2514/1.47317

N. Wereley
Associate Editor